# Comparison of the activities of $C_2N$ and BCNO towards Congo red degradation

Roberto C. Dante[1*], Pablo Martín-Ramos[2], Pedro Chamorro-Posada[3], Siwaporn Meejoo-Smith[4], José Vázquez-Cabo[5], Óscar Rubiños-López[5], Luis Lartundo-Rojas[6], Francisco M. Sánchez-Árevalo[7], Jirawat Trakulmututa[3], Dario Rutto[8], Siraprapha Deebansok[3] and Assadawoot Srikhaow[3]

[1] Research, Development & Innovation, 2Dto3D S.r.l.s. Via Revalanca 5, 12036 San Firmino, Revello (CN), Italy. E-mail: rcdante@2dto3dmaterials.com

[2] EPS, Universidad de Zaragoza, Carretera de Cuarte s/n, 22071, Huesca, Spain

[3] Dpto. de Teoría de la Señal y Comunicaciones e IT, Universidad de Valladolid, ETSI Telecomunicación, Paseo Belén 15, 47011 Valladolid, Spain.

[4] Faculty of Science, Mahidol University, 999 Phuttamonthon Sai 4 Road, Salaya, Phuttamonthon, Nakorn Pathom 73170, Thailand.

[5] Dpto. de Teoría de la Señal y Comunicaciones, Universidad de Vigo, ETSI Telecomunicación, Lagoas Marcosende s/n, Vigo, Spain.

[6] Instituto Politecnico Nacional, Centro de Nanociencias y Micro y Nanotecnologías de Nanociencias, UPALM, Zacatenco, Mexico City, 07738, Mexico.

[7] Instituto de Investigaciones en Materiales, Universidad Nacional Autónoma de México, Apdo. Postal 70-360, Cd. Universitaria, Mexico City 04510, Mexico.

[8] R&D Department, Burgo Group, Via Roma 10, 12039 Verzuolo (CN), Italy

**Abstract**

An *n*-type organic carbon nitride semiconductor, $C_2N$, was synthesized by the pyrolysis of uric acid, and its properties were investigated by scanning electron and transmission electron microscopies, X-ray powder diffraction, and vibrational, UV-visible and X-ray photoelectron spectroscopies. This novel material, composed of crystalline flakes, featured a broad absorption centered at 700 nm, possibly due to charge transfer, and a 2.49 eV band gap. Its catalytic performance was assessed for the treatment of effluents with the diazo dye Congo red, comparing it with that of boron carbon nitrogen oxide, BCNO. Both wide band gap semiconductors exhibited decolorizing activity in the dark, although the mechanisms were different and were not photocatalytic: BCNO was more effective towards the adsorption-coordination due to the presence of B-O, while $C_2N$ was effective towards the adsorption and the advancement of the oxidation reaction. Their kinetic constants (0.19 and 0.02 $min^{-1}$ for BCNO and $C_2N$, respectively) were comparable to those of intermetallic compounds studied for azo dyes degradation in dark conditions. In view of the high color removal efficiency (97% after 20 min) and good reusability of BCNO, this study suggests a potential application of this catalyst for wastewater treatment, alone or in combination with $C_2N$.

**Keywords**: BCNO, $C_2N$, catalytic degradation, dye, organic semiconductor.

## 1. Introduction

In recent years, semiconductor-based materials have found one of their key applications in the degradation of contaminants. The removal of biological and organic/inorganic water pollutants has become a burgeoning field of research [1, 2]. Carbon-based materials (viz. single wall carbon nanotubes (SWCNTs), multiwall carbon nanotubes (MWCNTs), mesoporous carbons, graphene, graphene oxide or biochar), as well as some of their nanocomposites, have been shown to hold great promise for water treatment and desalination [3-8]. Nonetheless, other metal-free semiconductors with a mild band gap, such as polymeric carbon nitride (g-$C_3N_4$) and

boron-nitride-based materials, have also found successful application in environmental pollution remediation [9-11].

After the pioneering work by Mahmood, Lee [12], layered multifunctional 2-D materials with $C_2N$ stoichiometry have also started to attract increasing attention. However, to date most papers have analyzed the applicability of such materials only from a theoretical perspective (making use of DFT and *ab-initio* simulations): e.g., for water splitting [13], for gas separation [14], for seawater desalination [15] or for the detection of gaseous pollutants [16].

In a previous experimental work, we reported that a material with a N to C atomic ratio ~0.6, featuring a polymer structure and electronic properties that differed from those of g-$C_3N_4$, could be obtained from the pyrolysis of a mixture of uric acid and melamine [17]. The characterization results suggested that such $C_2N$ would be a polymeric semiconductor, featuring a very organized 2-D supramolecular structure, with a diffused and strong network of hydrogen bonds. This layered carbon-nitrogen material contained imidazole-, pyridine (naphthyridine)- and graphitic-like nitrogen. The newly synthesized material presented herein was obtained in a similar way to that reported in [17], but in this case no melamine was added to the reaction blend, in such a way that the resulting material was obtained only from the pyrolysis of pure uric acid. Although it was expected to be similar to the previously reported one, it was found to exhibit new and dissimilar properties.

In view of the limited availability of experimental assessments of the applicability of this novel class of materials, in this paper we have explored the adsorption and catalytic activity of this new carbon nitride $C_2N$ material by making a comparison with boron carbon nitrogen oxide (BCNO), a previously characterized and discussed material [18]. Congo red (CR) dye degradation has been monitored under UV light, UV-Visible light and in dark conditions.

## 2. Experimental

### 2.1. *Materials*

Uric acid (CAS No. 69-93-2), urea (CAS No. 57-13-6) and boric acid (CAS No. 10043-35-3) were supplied by Alfa Aesar (Karlsruhe, Germany) with purities higher than 99%, and were used for the synthesis without further purification.

### 2.2. *Synthesis*

For the preparation of $C_2N$, 15 g of uric acid (UA) were treated at 580 °C for 30 min. The reaction yield was *ca.* 30 wt%. BCNO was prepared by reaction of 25 g of urea with 5 g of boric acid at 580 °C for 30 min. The reaction yield was *ca*. 13 wt%.

### 2.3. *Characterization*

The vibrational spectra were collected with a Carey 630 Fourier-Transform Infrared (FTIR) spectrometer (Agilent Technologies, Santa Clara, CA, USA). FTIR spectra were obtained directly from the materials in powder form using an in-built diamond Attenuated Total Reflection (ATR) system, at a 1 $cm^{-1}$ spectral resolution and with 64 scans.

Scanning electron microscopy (SEM) and transmission electron microscopy (TEM) micrographs were obtained with a FEI (Hillsboro, Oregon, USA) QUANTA 200F and with a JEM-2010F and a JEM-1010 (JEOL, Akishima, Tokyo, Japan) apparatus, respectively, so as to retrieve information of the particles morphology. In order to determine the interplanar distance from the TEM micrographs, the “Process/FFT” (Fast Fourier Transformation) tool available in ImageJ [19] was used. The obtained value was corroborated by an alternative procedure in the same software: a straight line perpendicular to the lattice fringe was drawn in the HRTEM image, the profile was plotted (as a "Gray Value" vs. "Distance" plot), and the distance between twenty or more peaks was averaged.

X-ray diffraction patterns were obtained with an ULTIMA-IV (Rigaki Corp., Tokyo, Japan) Bragg-Brentano powder diffractometer with Cu-Kα radiation, using crystalline silicon as a standard. The interplanar distance (in Å) was calculated from Bragg's law: $d = \lambda/\{2 \sin [0.5(2\theta)]\}$, taking $\lambda$=1.5406 Å [20].

UV-Vis diffuse reflectance spectra were measured with a Lambda 35 UV-Vis spectrophotometer (Perkin Elmer Inc., Waltham, MA, USA), taking a Spectralon® blank as a reference. Transformation of reflectance data into absorbance data was conducted using the Kubelka-Munk method: $F(R)(1-R)^2/2R$, where $R$ is the reflectance and $F(R)$ is the Kubelka-Munk function. The band gap was estimated through a Tauc plot [21, 22].

In relation to the elemental composition and chemical species in the $C_2N$ specimens, they were determined using a K-alpha (Thermo Fischer Scientific, Waltham, MA, USA) X-ray photoelectron spectrometer (XPS) system with a monochromatic Al-Kα radiation X-ray source (1486.6 eV). X-rays were microfocused to give a 400 μm in diameter spot size on the sample. The analyzer was run in constant analyzer energy mode. XPS survey and high resolution spectra were collected using analyzer pass energies of 100 and 20 eV, respectively. In order to compensate for effects related with charge shift, C1s peak at 284.6 eV was used as an internal standard. The samples remained in the pre-chamber for 15 h and were then transferred to the analytical chamber with a base pressure of $1\times10^{-9}$ Torr. Core level spectra were deconvoluted using a Shirley-type background subtraction and a pseudo-Voigt function (Gaussian (70%) – Lorentzian (30%) mixing) fitting for each component in Avantage v5.97 software.

### 2.4. *Catalytic activity and adsorption tests*

To determine the efficiency in dye removal, 10 mg of catalyst, either $C_2N$ or BCNO, were added to 10 mL of a 20 ppm aqueous solution of Congo red (CR). The suspensions were stirred in the dark and, at given time intervals, the reaction was terminated by filtering using 0.45 μm syringe filter to separate the catalyst from the medium. The concentration of CR was measured using a GENESYS 10S (Thermo Fisher Scientific) UV–Vis spectrophotometer at 498 nm. The efficiency of color removal was calculated according to Eq. 1.

$$\text{Color removal efficiency (\%)} = \frac{C_0 - C_t}{C_0} \times 100 \quad (1)$$

where $C_0$ is the initial concentration of CR and $C_t$ is the concentration of CR after $t$ minutes of treatment. Other tests were performed at 35 °C (lamp distance: 10 cm from the test tube) with UV-Vis and Vis light sources (UV-vis: OSRAM Ultra-vitalux 2×300 W; Vis: four LED lamps with 4×40 W) in order to highlight the importance of the photocatalytic formation of radicals in the process of CR degradation. The reusability of the two catalysts was assessed by several consecutive adsorption-desorption cycles, without any regeneration (i.e., washing) in-between cycles.

## 3. Results and discussion

### 3.1. *Structural and physical-chemical characterization*

#### 3.1.1. *Vibrational analysis of $C_2N$ and UA*

The ATR-FTIR spectrum of UA (see Figure 1) was dominated by the absorption band associated with NH, OH, and carbonyl CO chemical groups. The two bands at 1650 and 1580 $cm^{-1}$, typical of secondary amides, resulted from the amidic carbonyl; whereas the band at *ca*. 3000 $cm^{-1}$ was connected to OH stretching vibrations, all interacting by hydrogen bond. A detailed assignations of bands can be found in a previous report by Dante *et al*. [17].

On the other hand, for the $C_2N$ compound one could observe that most bands associated with OH, CO and NH groups had disappeared or had almost disappeared (in the case of the OH stretching bands). The bands at 1580 and 1240 $cm^{-1}$ could be ascribed to vibrations of rings containing 6-5 nitrogen atoms: the band at 1580 $cm^{-1}$ may be related to ring stretching vibrations

from both pyridine-like and imidazole (or pyrrole)-like rings, while C-N stretching of imidazole-like rings would generate the band at 1240 $cm^{-1}$. From this point of view, the infrared spectrum would be similar to that previously obtained for nitrogen-doped graphene [17, 23-25].

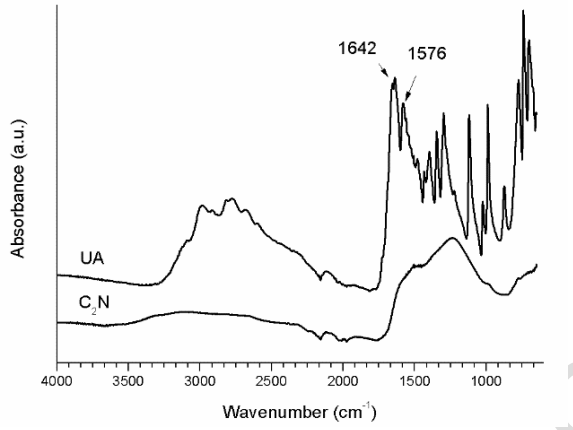


**Figure 1.** ATR-FTIR spectra of uric acid (UA) and carbon nitride ($C_2N$) obtained at 600 °C.

3.1.2. *Morphology of the products: SEM and TEM analysis*

Small amounts of the products were suspended in ethanol, sonicated and a fraction of the suspended material was observed in a SEM. Micrographs representative of the two pyrolysis products are shown in Figure 2.

Rectangular tablet particles with tiny pores below the micrometric size characterized the material synthesized from uric acid ($C_2N$). In addition, it was possible to distinguish the stacked lamellae that composed the particles. On the other hand, BCNO was mostly composed by irregular particles with micropores. The porous structure of BCNO seemed to be due to coalescence of small particles.

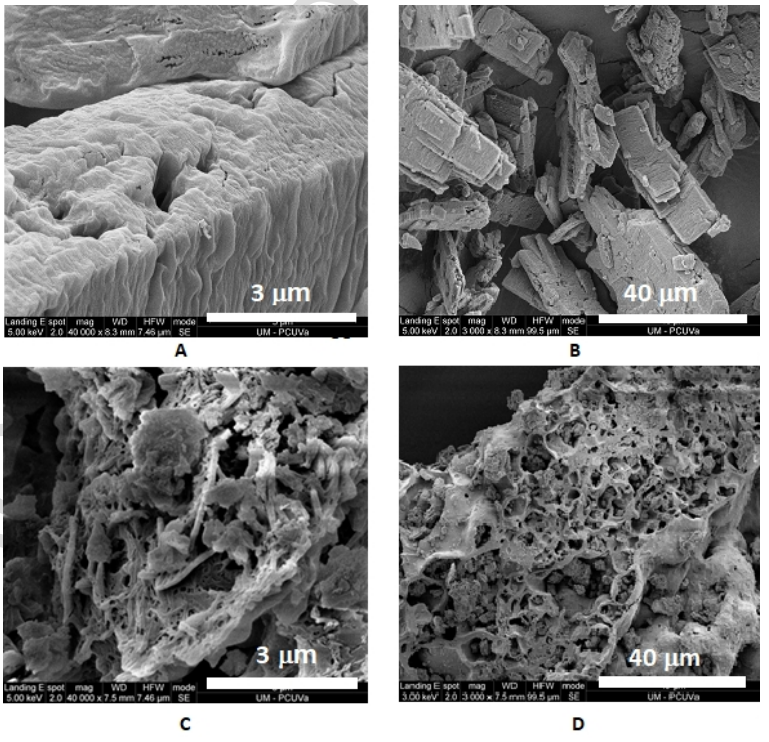


**Figure 2.** SEM micrographs of $C_2N$ (*A* and *B*) and of BCNO (*C* and *D*).

The TEM analysis of the $C_2N$ material showed an area with a considerable degree of order surrounded by large disordered regions, as depicted in Figure 3. An interplanar distance of 3.38 Å (0.338 nm) was determined, which was in accordance with the (002) reflection of graphite and with the XRD results, discussed below. Apropos of the TEM of BCNO, it did not show any relevant features compared to those found by SEM.

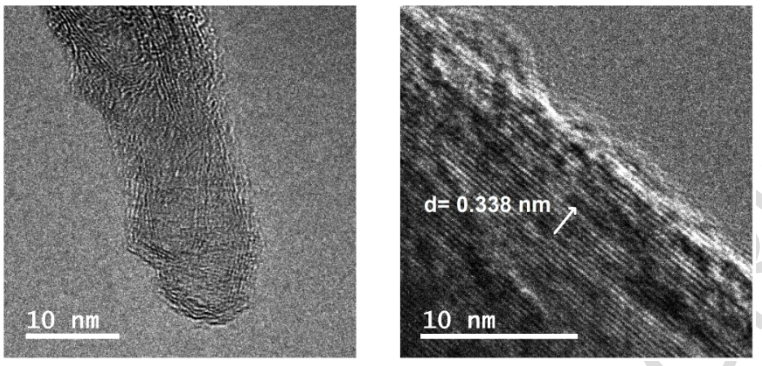


**Figure 3.** TEM micrographs of the diffraction planes for the $C_2N$ sample.

3.1.3. *X-ray diffraction measurements*

The powder XRD pattern of the $C_2N$ material showed the characteristic peaks of low degree of crystallinity turbostratic carbon materials such as coke: a (002) reflection at 26.33°, corresponding to an interplanar distance of 3.38 Å, and a reflection at 13.13°, corresponding to a spacing 6.73 Å, which can be ascribed to (001) reflection (see Figure 4).

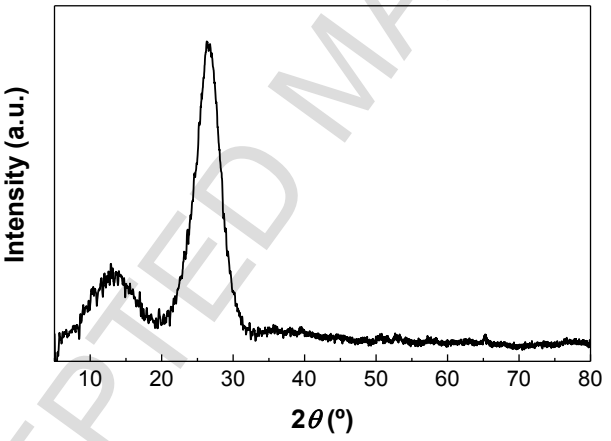


**Figure 4.** X-ray powder diffraction pattern of $C_2N$ sample.

Although the (002) peak of $C_2N$ was very close to that of a crystalline graphite, it should be noticed that whereas graphite is a well-organized material with sharp reflections, $C_2N$ is an amorphous one, as it may be argued by the broad peaks.

Other nitrogen-doped graphene or graphitic materials also feature the diffraction peak at around 27°. In fact, Horibe *et al*. found that the interplanar distance monotonously decreased as the N/C content ratio increased [26, 27]. However, other factors must be considered, provided that in pure carbon materials the interplanar distance can vary from 3.37 to 3.50 Å depending on the degree of layer-ordered stacking.

The obtained material was very similar to those synthesized by Xu *et al*. from hexa-aminobenzene, surprisingly both in morphology and XRD pattern, and in the C/N ratio as determined by XPS. These analogies about the synthesis of very similar products starting from different reagents made us think that we were dealing with a specific new compound, instead of a graphite with a high content of nitrogen as Xu, Mahmood [28] supposed. Otherwise, it would

be impossible that same ratios of N to C, same XPS, XRD and particle morphologies could be obtained from different reagents. This would be similar to what happens with g-$C_3N_4$, which can be obtained from different reagents, but the final product is always the same [29-33]. This fact would reinforce our hypothesis that the material is more probably a polymer with imidazole and naphtapyridinic units [18].

### 3.1.4. *UV-visible spectroscopy*

The UV-Vis spectrum of $C_2N$ is depicted in Figure 5. It was possible to see two absorptions, one at lower wavelength values (below 500 nm) that would be connected to the valence band to the conduction band transition ($\pi \rightarrow \pi^*$), while the other broad band around 700 nm may be due to charge transfer. In fact, adjacent chains interacting by hydrogen bond can form charge transfer complexes with the exchange of the hydrogen atoms of the imidazole. Moreover, since a certain amount of oxygen was still present in the material, the formation of acceptor and donor pairs could be favored. This charge transfer effect can become sharper as the degree of order increases. The optical band gap for the indirect transition was 2.49 eV, as determined by Tauc plot. This band gap value was lower than that of BCNO, which was 3.22 eV, as already reported in [18].

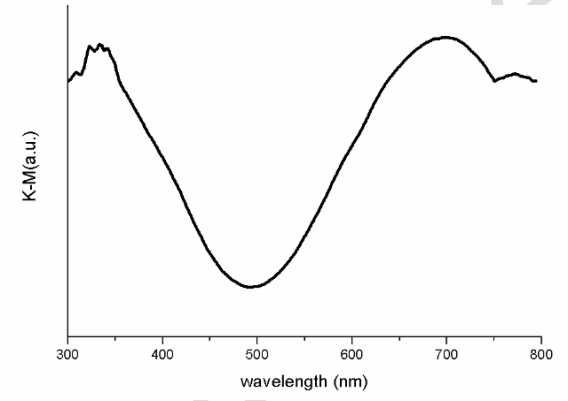


**Figure 5.** UV-visible Kubelka-Munk transformed diffuse reflectance spectrum of $C_2N$.

### 3.1.5. *X-ray photoelectron spectroscopy analysis*

The surface elemental and chemical composition of the $C_2N$ sample was determined by XPS analysis. The XPS survey and high resolution C1s and N1s regions were obtained. In Figure 6, the survey spectrum of the $C_2N$ sample is presented and from this it was possible to identify and quantify the different picks associated to C1s, N1s and O1s (Table 1).

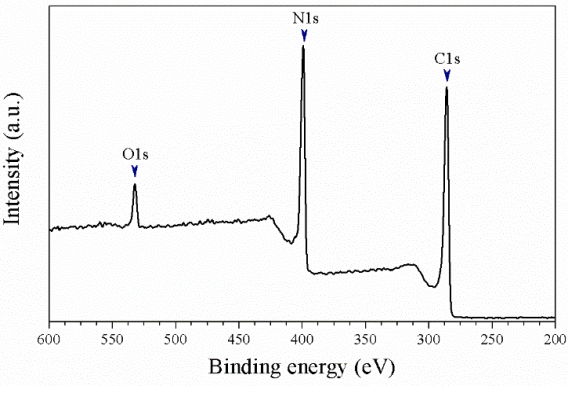


**Figure 6.** XPS survey spectrum of the $C_2N$ sample, in which C1s, N1s and O1s XPS peaks are identified.

**Table 1.** Estimated elemental carbon, nitrogen and oxygen contents for $C_2N$ sample.

| Element | wt% |
|---|---|
| C1s | 57.1 |
| N1s | 36.0 |
| O1s | 6.6 |

The C1s high resolution spectrum is shown in Figure 7. The spectrum was fitted by eight Gaussian-Lorentzian contributions with binding energies (BE) centered at 284.5, 284.9, 285.6, 286.4, 287.2, 288.1, 290.8 and 292.3 ± 0.2 eV, associated with C-C and $sp^2$ (C=C) (C1), C-N (pyridinic, naphthyridinic) (C2), C-N-H (C3), C=O (C4), imidazolic C=N (C5), -COOH, -O-C=O (C6), π-π* (C7) and O-C(=O)-O (C8), respectively. The corresponding BE and relative mass fraction (wt%) of each contribution are listed in Table 2.

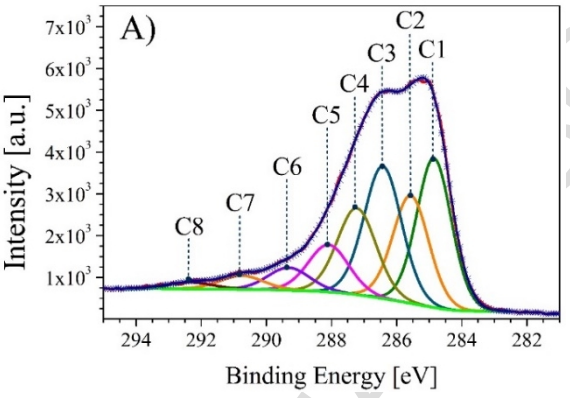


**Figure 7.** Deconvoluted high resolution XPS spectra of C1s region of $C_2N$.

**Table 2.** Binding energies (±0.2 eV) and chemical species quantification results of C1s and N1s due to the specific bonds of $C_2N$ sample.

| (Elemental wt%) | C 1s (57.1) | | | | | | | |
|---|---|---|---|---|---|---|---|---|
| Peak | C1 | C2 | C3 | C4 | C5 | C6 | C7 | C8 |
| BE ± 0.2 eV | 284.5 | 284.9 | 285.6 | 286.4 | 287.2 | 288.1 | 289.3 | 290.8 |
| wt% | 24.4 | 18.4 | 23.5 | 16.0 | 9.0 | 4.5 | 2.8 | 1.4 |
| (Elemental wt%) | N 1s (36.0) | | | | | | | |
| Peak | N1 | N2 | N3 | N4 | N5 | N6 | N7 | - |
| BE ± 0.2 eV | 398.3 | 398.8 | 399.6 | 400.4 | 401.2 | 402.7 | 404.9- | - |
| wt% | 23.3 | 25.0 | 16.5 | 20.9 | 9.7 | 2.4 | 2.3 | - |

After a fitting processing of the high resolution N1s region, 395.0–407.0 eV, the presence of seven nitrogen species was evinced. In Figure 8, the Gaussian-Lorentzian contributions for the nitrogen chemical species referred to as: N pyridinic (naphthyridinic) (N1), C-NH imidazolic (N2), nitrile, pyrrolic-N (N3), C-N-C imidazolic (N4), graphitic N, C-O-N (N5), N oxidation (N6), and $\pi$-$\pi^*$ (N7), respectively, are presented. The nitrogen species peak position and relative weight percent (wt%) are summarized in Table 2.

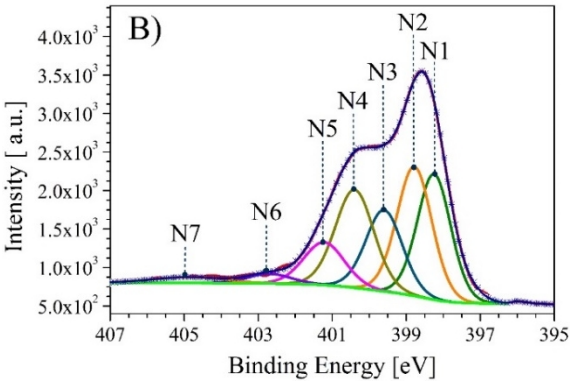


**Figure 8.** Deconvoluted high resolution XPS spectra of N1s region of $C_2N$.

The spectrum of XPS low binding energy regions of $C_2N$ and BCNO, shown in Figure 9, allowed us to determine the energy difference between the valence band and the energy of the Fermi level, as well as the difference between the energy of the conduction band and that of the Fermi Level, by means of the optical band gap energy. The position of the Fermi levels close to the conduction band indicated that both materials were *n* type semiconductors (see Figure 10), i.e., with many electrons from donors with energies close to the conduction band.

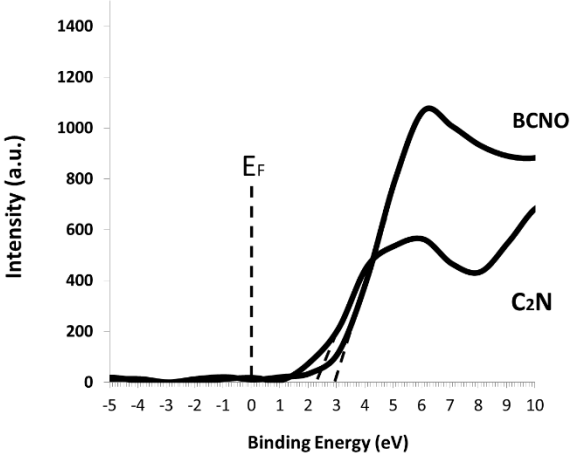


**Figure 9.** Valence bands cut-off of $C_2N$ and BCNO. The intersection of the dashed lines with binding energy axis corresponds to the valence band energy.

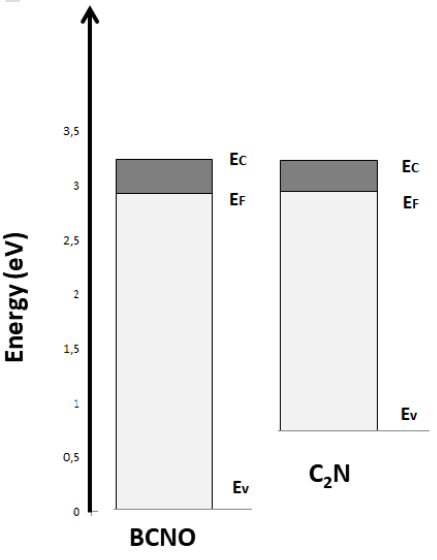


**Figure 10.** Energy gap components of $C_2N$ and BCNO. $E_c$, $E_v$ and $E_F$ stand for the lowest energy level of

the conduction band, the highest energy level of the valence band and the energy of the Fermi level, respectively.

### 3.2. *Catalytic activity*

The color removal of a 20 ppm CR solution by using BCNO and $C_2N$ in dark conditions is reported in Figure 11. The removal efficiency of BCNO achieved 97% of the initial concentration, while that of $C_2N$ achieved 52% after 20 min.

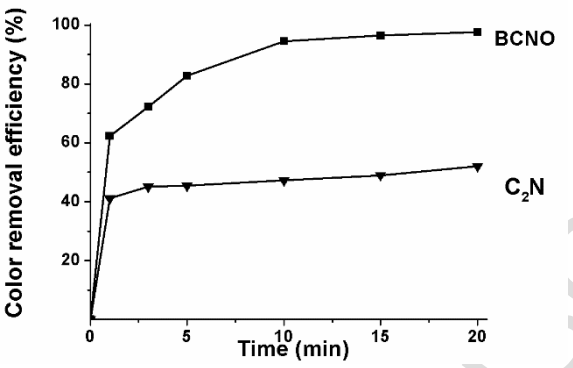


**Figure 11.** Efficiency of color removal of 10 mL solution of 20 ppm of Congo red (CR) by 10 mg of BCNO and $C_2N$ catalysts.

The surface areas of the two materials, determined by Brunauer–Emmett–Teller (BET), were 22.37 and 33.6 $m^2 \cdot g^{-1}$ for BCNO and $C_2N$, respectively. In the absence of detailed information on the micro/mesopores volume, the fact that the surface area of $C_2N$ was higher than that of BCNO suggested that the better performance of BCNO should not be ascribed to adsorption mechanisms. In addition, experiments with visible and UV-Vis light did not show a different behavior from the ones in the dark. This implied that the main mechanism was not photocatalytic either. Moreover, tests with a radical scavenger (isopropyl alcohol) showed a *ca.* 10% lower efficiency in color removal due to the scavenger interference for BCNO, and a *ca.* 15% lower efficiency for $C_2N$, both in 20 min of reaction with a molar ratio of isopropyl alcohol to CR of 1000:1 (see Figure 12). Since the scavenger effect was more marked for $C_2N$, the degradation mechanism of $C_2N$ would then be possibly more connected to the formation of oxygen radicals that would oxidize the CR azo dye [34].

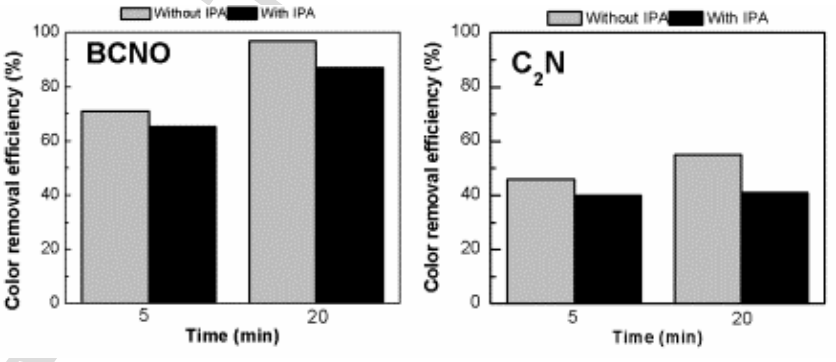


**Figure 12.** Color removal efficiency tests with and without the radical scavenger isopropyl alcohol (IPA).

BCNO was probably more effective towards the adsorption of the azo dye CR because of the presence of boron and B-O bonds. Boron sites are Lewis acid ones, which can attract and cleave azo bonds, favoring further reactions involving the nitrogen atoms. The cleavage products showed intense adsorptions below 300 nm, as shown by the UV-Vis spectra of the solution (see

Figure 13), which is compatible with both benzenic and naphtalenic amine byproducts. The shoulder at 272 nm grew along the test and may correspond to the naphthalene amine byproducts (the azo bonds to be broken are two in CR). In few words, the cleavage of the azo bond suddenly shifted the benzene and naphtalene absorption to wavelengths below 300 nm. The degradation mechanism for BCNO ought to be very similar to that of reagents such as metals which provide electrons to form aromatic amines [35].

Figure 13 shows the UV-Vis absorption spectra in the 200 to 800 nm range as a function of time for the 20 ppm CR solutions treated with the adsorbents/catalysts. It is worth noting that in the case of $C_2N$ there was no evident UV-Vis absorption due to aromatic byproducts, suggesting that the adsorption process would be dominant, and possibly that the oxidation proceeded to spectroscopically inactive species. In the case of BCNO, a strong band below 300 nm appeared due to the treatment, and the shoulder at 272 nm increased due to the formation of aromatic byproducts.

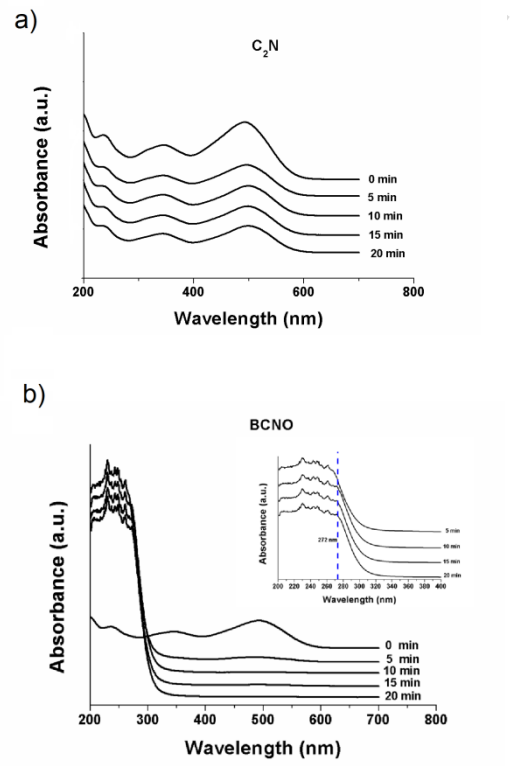


**Figure 13.** Time evolution of the UV-Vis absorption spectra during the Congo red (CR) degradation assays. Tests were conducted on 10 mL of solution with 20 ppm of CR treated with 10 mg of (a) $C_2N$ and (b) BCNO catalysts. The inset in (b) shows a zoom-in of the absorption spectrum in the range between 200 and 400 nm in the time interval between 5 and 20 min. The dashed vertical line highlights the growth of the shoulder at 272 nm**.**

### 3.2.1. *Analysis of adsorption kinetics*

The pseudo-first-order kinetic model applied to BCNO and $C_2N$ resulted in kinetic constants of 0.19 $min^{-1}$ and 0.02 $min^{-1}$, respectively, as it can be seen in Figure 14, which are values comparable to those of intermetallic compounds studied for the degradation of azo-dyes in dark conditions [36]. BCNO would act not only as an adsorbent but also as a reducing agent towards the azo-dye. The reaction may be favored by the Lewis acid characteristics and reducing properties of boron. Since boron as a dopant would increase the presence of holes close to the valence band (usually occurring only by thermal energy at room temperature) the scheme in Figure 15 depicts the reduction of the azo-dye as a consumption of electrons and holes localized nearby the boron sites. On the other hand, $C_2N$, an *n*-type semiconductor, seemed to be more effective towards adsorption. In Figure 15, following a similar scheme to that of BCNO, this mechanism is depicted as an adsorption on hole sites, close to the conduction band (hole sites are very localized in organic semiconductors). In addition, a certain degree of oxidation of CR would be due to oxygen radicals formed on the sites. Indeed, the hole radical scavenger effect was proportionally higher with $C_2N$. This interpretation may explain why no significant difference was found between light and dark experiments. In few words, the two materials were found to be suitable to work in dark conditions without the addition of metals and co-catalysts. Since their degradation mechanisms are very different, it is possible that they may be used together to cleave the azo bonds and adsorb the whole dye.

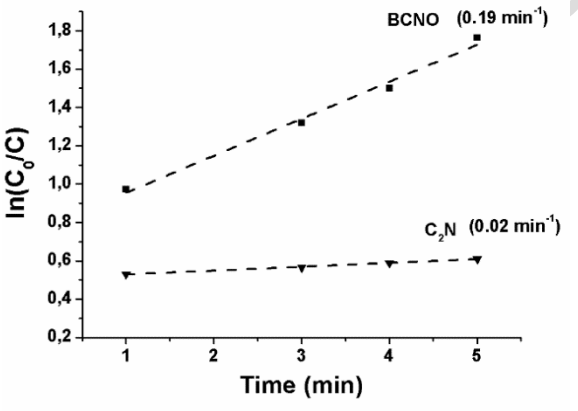


**Figure 14.** Pseudo first-order-kinetic model applied to the tests conducted on 10 mL of solution with 20 ppm of Congo red (CR) treated with 10 mg of BCNO and $C_2N$ catalysts.

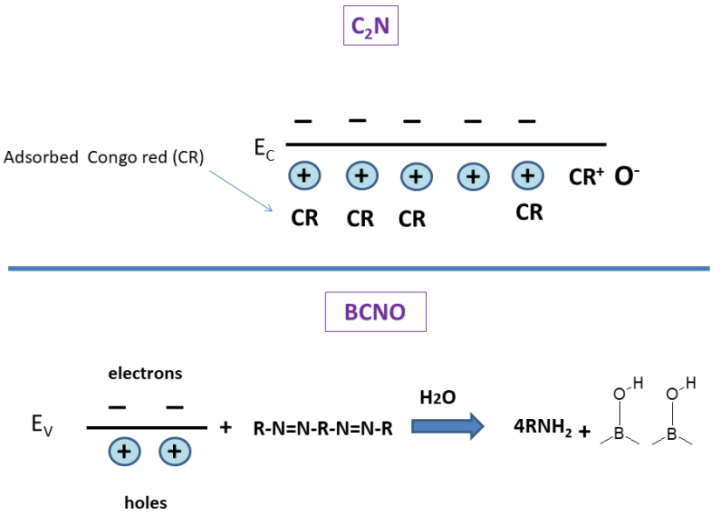

**Figure 15.** Possible mechanisms of CR degradation in the dark mediated by $C_2N$ (*top*) and BCNO (*bottom*) catalysts.

### 3.2.2. *Cycling of the two adsorbents*

Cycling of adsorbents is essential in practical applications, as a result of the economic and ecological demands for sustainability. Consequently, after adsorption of the CR dye by the two catalysts, their reusability was assessed by several consecutive adsorption-desorption cycles (

Figure 16), without any regeneration treatment in-between cycles. In the case of $C_2N$, the efficiency of dye removal dropped from 52% to *ca*. 40% after three cycles. No more cycles followed due to the dramatic drop in only three cycles. On the other hand, for BCNO it could be observed that, after an initial decrease from 97.3% (1st cycle) to 85.7% (2nd cycle), the material maintained most of its adsorption ability for CR even after 7 consecutive cycles (74.5%), and that the color removal efficiency after 9 cycles remained close to 65%. It should be noted that the gradual decrease could be partly due to handling losses of BCNO powder. The high absorbance capacity, the recyclability and the absorption kinetics of BCNO thus suggest that it would have more potential in industrial applications than $C_2N$.

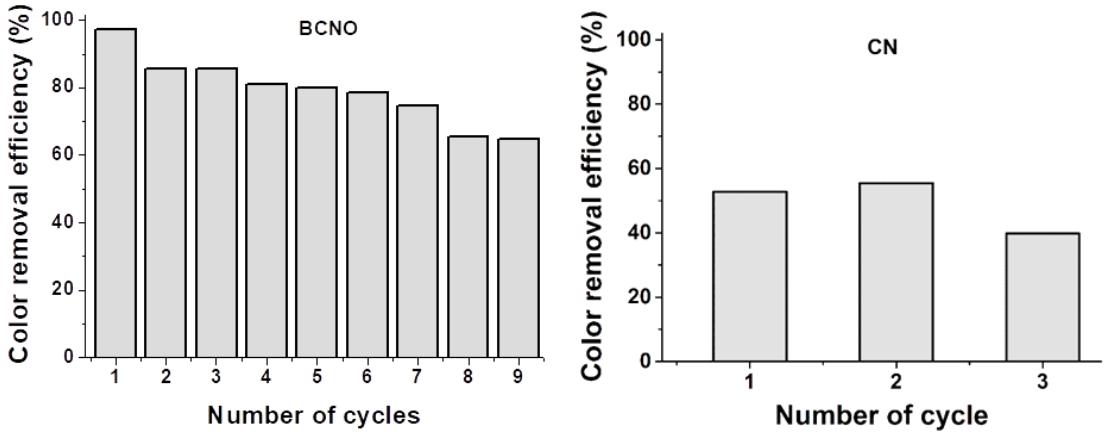


**Figure 16.** Recycling of BCNO (*left*) and $C_2N$ (*right*), with removal efficiency values after 20 min. The initial concentration of CR was 20 ppm and the amount of catalyst used was 10 mg in both cases. The catalysts were not regenerated in-between cycles.

## 4. Conclusions

Congo red dye degradation in different conditions was assessed using two *n*-type wide-band organic semiconductors: previously reported BCNO and a novel material synthesized by pyrolysis of uric acid, the carbon nitride $C_2N$. This latter material, with a high nitrogen content (~33 at%), was studied by ATR-FTIR, SEM, TEM, XRPD, UV-Vis and XPS spectroscopies. $C_2N$, composed of small square flakes with crystalline regions, exhibited a broad UV-Vis absorption centered at 700 nm, possibly due to charge transfer, and featured a 2.49 eV band gap, smaller than that of BCNO (3.22 eV). Both catalysts proved to be able to degrade the recalcitrant dye in dark conditions without the addition of metals and/or co-catalysts, albeit in a different manner and with distinct efficiencies: BCNO cleaved the azo bonds to form benzene and naphtalene compounds, while $C_2N$ favored adsorption, attaining color removal efficiencies of 97% and 52% after 20 min, respectively. In spite of the higher BET of $C_2N$ as compared to BCNO (33.6 *vs*. 22.37 $m^2 \cdot g^{-1}$, respectively), BCNO-mediated discoloration was noticeably faster than that of $C_2N$, with pseudo-first order kinetic constants of 0.19 and 0.02 $min^{-1}$, respectively.

Since the value for BCNO was comparable to those of intermetallic compounds studied for the degradation of azo-dyes in dark conditions, and given that it showed only a moderate loss in adsorption capacity after 9 cycles without any sort of regeneration treatment, it may hold promise for effluent treatment, separately or in combination with $C_2N$. Further research on their synergistic effect is under way.

## 5. Competing interest statement

The authors have no competing interests to declare.

## 6. References


1. Bora, L.V. and R.K. Mewada, *Visible/solar light active photocatalysts for organic effluent treatment: Fundamentals, mechanisms and parametric review.* Renewable and Sustainable Energy Reviews, 2017. **76**: p. 1393-1421. DOI: 10.1016/j.rser.2017.01.130.
2. Opoku, F., et al., *Recent Progress in the Development of Semiconductor-Based Photocatalyst Materials for Applications in Photocatalytic Water Splitting and Degradation of Pollutants.* Advanced Sustainable Systems, 2017. **1**(7). DOI: 10.1002/adsu.201700006.
3. Smith, S.C. and D.F. Rodrigues, *Carbon-based nanomaterials for removal of chemical and biological contaminants from water: A review of mechanisms and applications.* Carbon, 2015. **91**: p. 122-143. DOI: 10.1016/j.carbon.2015.04.043.
4. Goh, K., et al., *Carbon nanomaterials for advancing separation membranes: A strategic perspective.* Carbon, 2016. **109**: p. 694-710. DOI: 10.1016/j.carbon.2016.08.077.
5. Libbrecht, W., et al., *Soft templated mesoporous carbons: Tuning the porosity for the adsorption of large organic pollutants.* Carbon, 2017. **116**: p. 528-546. DOI: 10.1016/j.carbon.2017.02.016.
6. Li, R., et al., *An overview of carbothermal synthesis of metal–biochar composites for the removal of oxyanion contaminants from aqueous solution.* Carbon, 2018. **129**: p. 674-687. DOI: 10.1016/j.carbon.2017.12.070.
7. Kumar, S., et al., *Two-dimensional carbon-based nanocomposites for photocatalytic energy generation and environmental remediation applications.* Beilstein Journal of Nanotechnology, 2017. **8**: p. 1571-1600. DOI: 10.3762/bjnano.8.159.
8. Daud, M., et al., *Graphene/layered double hydroxides nanocomposites: A review of recent progress in synthesis and applications.* Carbon, 2016. **104**: p. 241-252. DOI: 10.1016/j.carbon.2016.03.057.
9. Mamba, G. and A.K. Mishra, *Graphitic carbon nitride ($g$-$C_3N_4$) nanocomposites: A new and exciting generation of visible light driven photocatalysts for environmental pollution remediation.* Applied Catalysis B: Environmental, 2016. **198**: p. 347-377. DOI: 10.1016/j.apcatb.2016.05.052.
10. Ding, F., et al., *Graphitic carbon nitride-based nanocomposites as visible-light driven photocatalysts for environmental purification.* Environmental Science: Nano, 2017. **4**(7): p. 1455-1469. DOI: 10.1039/c7en00255f.
11. Yu, S., et al., *Boron nitride-based materials for the removal of pollutants from aqueous solutions: A review.* Chemical Engineering Journal, 2018. **333**: p. 343-360. DOI: 10.1016/j.cej.2017.09.163.
12. Mahmood, J., et al., *Nitrogenated holey two-dimensional structures.* Nature Communications, 2015. **6**: p. 6486. DOI: 10.1038/ncomms7486.
13. Ashwin Kishore, M.R. and P. Ravindran, *Tailoring the Electronic Band Gap and Band Edge Positions in the C2N Monolayer by P and As Substitution for Photocatalytic Water Splitting.* The Journal of Physical Chemistry C, 2017. **121**(40): p. 22216-22224. DOI: 10.1021/acs.jpcc.7b07776.
14. Deng, S., et al., *A strain-controlled C 2 N monolayer membrane for gas separation in PEMFC application.* Applied Surface Science, 2018. **441**: p. 408-414. DOI: 10.1016/j.apsusc.2018.02.042.

15. Liu, B., A.W.-K. Law, and K. Zhou, *Strained single-layer C 2 N membrane for efficient seawater desalination via forward osmosis: A molecular dynamics study.* Journal of Membrane Science, 2018. **550**: p. 554-562. DOI: 10.1016/j.memsci.2017.10.067.
16. Bhattacharyya, K., S.M. Pratik, and A. Datta, *Controlled Pore Sizes in Monolayer C2N Act as Ultrasensitive Probes for Detection of Gaseous Pollutants (HF, HCN, and H2S).* The Journal of Physical Chemistry C, 2018. **122**(4): p. 2248-2258. DOI: 10.1021/acs.jpcc.7b11963.
17. Dante, R.C., et al., *Nitrogen-carbon graphite-like semiconductor synthesized from uric acid.* Carbon, 2017. **121**: p. 368-379. DOI: 10.1016/j.carbon.2017.05.098.
18. Rivera-Tapia, E.D., et al., *Synthesis of boron carbon nitride oxide (BCNO) from urea and boric acid.* Fullerenes, Nanotubes and Carbon Nanostructures, 2015. **24**(1): p. 8-12. DOI: 10.1080/1536383x.2015.1078794.
19. Schneider, C.A., W.S. Rasband, and K.W. Eliceiri, *NIH Image to ImageJ: 25 years of image analysis.* Nature Methods, 2012. **9**: p. 671. DOI: 10.1038/nmeth.2089.
20. Poppe, L., et al., *A laboratory manual for X-ray powder diffraction.* US Geological Survey Open-File Report, 2001. **1**(041): p. 1-88.
21. Tauc, J., R. Grigorovici, and A. Vancu, *Optical properties and electronic structure of amorphous germanium.* Physica Status Solidi B: Basic Solid State Physics, 1966. **15**(2): p. 627-637. DOI: 10.1002/pssb.19660150224.
22. Tauc, J., *Optical properties and electronic structure of amorphous Ge and Si.* Materials Research Bulletin, 1968. **3**(1): p. 37-46. DOI: 10.1016/0025-5408(68)90023-8.
23. Zhang, Y., et al., *Nitrogen-doped graphene as a cathode material for dye-sensitized solar cells: effects of hydrothermal reaction and annealing on electrocatalytic performance.* RSC Adv., 2015. **5**(14): p. 10430-10439. DOI: 10.1039/c4ra13224f.
24. Indrawirawan, S., et al., *Low temperature combustion synthesis of nitrogen-doped graphene for metal-free catalytic oxidation.* J. Mater. Chem. A, 2015. **3**(7): p. 3432-3440. DOI: 10.1039/c4ta05940a.
25. Wang, G., et al., *Novel preparation of nitrogen-doped graphene in various forms with aqueous ammonia under mild conditions.* RSC Advances, 2012. **2**(30): p. 11249. DOI: 10.1039/c2ra21348f.
26. Soo, L.T., et al., *The effect of varying N/C ratios of nitrogen precursors during non-metal graphene catalyst synthesis.* International Journal of Hydrogen Energy, 2016. DOI: 10.1016/j.ijhydene.2016.06.033.
27. Horibe, T., et al., *Molecular routes syntheses of graphite-like C-N compounds with various N/C ratios in high pressure and temperature.* Journal of the Ceramic Society of Japan, 2016. **124**(10): p. 1013-1016. DOI: 10.2109/jcersj2.16123.
28. Xu, J., et al., *2D frameworks of $C_2N$ and $C_3N$ as new anode materials for lithium-ion batteries.* Advanced Materials, 2017. **29**(34). DOI: 10.1002/adma.201702007.
29. Li, X., et al., *Preparation and characterization of graphitic carbon nitride through pyrolysis of melamine.* Applied Physics A, 2008. **94**(2): p. 387-392. DOI: 10.1007/s00339-008-4816-4.
30. Dante, R.C., et al., *Synthesis under pressure of potential precursors of CNx materials based on melamine and phenolic resins.* Journal of Macromolecular Science, Part B, 2010. **49**(2): p. 371-382. DOI: 10.1080/00222340903355859.
31. Zhang, Y., T. Mori, and J. Ye, *Polymeric carbon nitrides: Semiconducting properties and emerging applications in photocatalysis and photoelectrochemical energy conversion.* Science of Advanced Materials, 2012. **4**(2): p. 282-291. DOI: 10.1166/sam.2012.1283.
32. Dante, R.C., et al., *Synthesis of graphitic carbon nitride by reaction of melamine and uric acid.* Materials Chemistry and Physics, 2011. **130**(3): p. 1094-1102. DOI: 10.1016/j.matchemphys.2011.08.041.
33. Martín-Ramos, P., et al., *A simple approach to synthesize g-$C_3N_4$ with high visible light photoactivity for hydrogen production.* International Journal of Hydrogen Energy, 2015. **40**(23): p. 7273-7281. DOI: 10.1016/j.ijhydene.2015.04.063.
34. Chen, H., et al., *Degradation of azo dye Orange II under dark ambient conditions by calcium strontium copper perovskite.* Applied Catalysis B: Environmental, 2018. **221**: p.

691-700. DOI: 10.1016/j.apcatb.2017.09.056.
35. Ben Mbarek, W., et al., *Rapid degradation of azo-dye using Mn–Al powders produced by ball-milling.* RSC Advances, 2017. **7**(21): p. 12620-12628. DOI: 10.1039/c6ra28578c.
36. Qin, X.D., et al., *Ultrafast degradation of azo dyes catalyzed by cobalt-based metallic glass.* Scientific Reports, 2015. **5**(1). DOI: 10.1038/srep18226.